

# Study of Accretion Flow Dynamics of V404 Cygni during its 2015

## Outburst

Arghajit Jana<sup>1,2</sup>, Jie-Rou Shang<sup>3</sup>, Dipak Debnath<sup>2</sup>, Sandip K. Chakrabarti<sup>2</sup>, Debjit Chatterjee<sup>2</sup> and Hsiang-Kuang Chang<sup>4</sup>

<sup>1</sup> Astronomy & Astrophysics Division, Physical Research Laboratory, Navrangpura, Ahmedabad 380009, India; *argha0004@gmail.com*

<sup>2</sup> High Energy Astrophysics, Indian Centre for Space Physics, Garia St Road, Kolkata 700084, India

<sup>3</sup> Institute of Astronomy, National Tsing Hua University, Hsinchu 30013, Taiwan

<sup>4</sup> Department of Physics, National Tsing Hua University, Hsinchu 30013, Taiwan

Received 20xx month day; accepted 20xx month day

**Abstract** The 2015 Outburst of V404 Cygni is an unusual one with several X-ray and radio flares and rapid variation in the spectral and timing properties. The outburst occurred after 26 years of inactivity of the black hole. We study the accretion flow properties of the source during its initial phase of the outburst using *Swift*/XRT and *Swift*/BAT data in the energy range of 0.5 – 150 keV. We have done spectral analysis with the two component advective flow (TCAF) model fits file. Several flow parameters such as two types of accretion rates (Keplerian disk and sub-Keplerian halo), shock parameters (location and compression ratio) are extracted to understand the accretion flow dynamics. We calculated equipartition magnetic field  $B$  for the outburst and found that the highest  $B \sim 900$  Gauss. Power density spectra (PDS) showed no break, which indicates no or very less contribution of the Keplerian disk component, which is also seen from the result of the spectral analysis. No signature of prominent quasi-periodic oscillations (QPOs) is observed in the PDS. This is due to the mismatch of the cooling timescale and infall timescale of the post-shock matter.

**Key words:** X-Rays:binaries – stars individual: (V404 Cygni) – stars:black holes – accretion, accretion disks – shock waves – radiation:dynamics

## 1 INTRODUCTION

Transient black hole candidates (BHCs) have two phases in their lives: quiescence phase and outbursting phase. They spend most of their lifetimes in the quiescence phase. Sudden rise in viscosity leads to an outburst when the X-ray intensity rises by a factor of thousands or more that of

this process, gravitational potential energy is converted to heat and radiation. Black hole (BH) spectra generally consist of two components: a multicolour blackbody bump and a hard power-law tail. The multicolour blackbody part is believed to originate from a Shakura-Sunyaev type standard thin disk (Shakura & Sunyaev 1973; Novikov & Thorne 1973). The power-law tail is believed to originate from a Compton corona (Sunyaev & Titarchuk 1980; Sunyaev & Titarchuk 1985). In the two component advective flow (TCAF) solution, the CENBOL or CENtrifugal pressure supported BOUNDary Layer (Chakrabarti 1995; Chakrabarti & Titarchuk 1995; Chakrabarti 1997) replaces the Compton corona used in other models such as disk-corona model (Zdziarski 1993; Haardt & Marschi 1993) or evaporated disk in ADAF (Narayan & Yi 1994; Esin et al. 1997). In this paper, we used the TCAF solution to study the accretion flow dynamics of V404 Cygni during its first outburst in 2015 after a long quiescent of  $\sim 26$  years.

V404 Cygni is one of the most studied black hole X-ray binary systems. It is also known as GS 2023+338. It was first identified as an optical nova in 1938 (Wachmann 1948). In 1956, another nova outburst was reported in this system (Ritcher 1989). In 1989, V404 Cygni went through another outburst. The 1989 outburst was discovered with the all sky monitor onboard Ginga (Makino 1989). It is located at RA =  $306^{\circ}.01$  and Dec =  $33^{\circ}.86$ . The 1989 outburst was studied extensively. On 2015 June 15, after long 26 years in quiescent, V404 Cygni went through a short but violent outburst. In Dec 2015, another short activity was observed (Barthelmy et al. 2015; Lipunov et al. 2015). The binary system V404 Cygni harbours a black hole of mass  $9 - 12 M_{\odot}$  at the centre with a K-III type companion of mass  $\sim 1 M_{\odot}$  (Casares et al. 1992; Shahbaz et al. 1994; Khargharia et al. 2010). The inclination angle of the binary system is  $\sim 67^{\circ}$  (Shahbaz et al. 1994; Khargharia et al. 2010). The orbital period of the system is 6.5 days (Casares et al. 1992). The binary system is located at a distance of 2.39 kpc, measured by parallax method (Miller-Jones et al. 2009). V404 Cygni has a high spinning black hole with spin parameters  $a^* > 0.92$  (Walton et al. 2017).

The 2015 outburst of V404 Cygni was discovered on June 15 simultaneously by *Swift*/BAT (Barthelmy et al. 2015) and *MAXI*/GSC (Negoro et al. 2015). During this outburst, the source was extensively observed in multi-wavelength bands, such as in radio (Mooley et al. 2015a; Trushkin et al. 2015b), optical (Gazeas et al. 2015) and X-ray ((Rodriguez et al. 2015); (Radhika et al. 2016)). *INTEGRAL* observation reported multiple X-ray flares during the outburst (Rodriguez et al. 2015). Several radio flares were also observed. The source showed rapid changes in the spectral properties in very short time (Motta et al. 2017). *INTEGRAL* observation detected  $e^- - e^+$  pair annihilation on June 20, 2015 (Siegert et al. 2016; Radhika et al. 2016). *FERMI*/LAT detected high energy  $\gamma$ -ray jet in the source on June 26, 2015 (Loh et al. 2016). King et al. reported detection of emission lines with Chandra-HETG, indicating strong disc wind emission (King et al. 2015)

In this *paper*, we study the timing and the spectral properties of V404 Cygni with combined *Swift* XRT and BAT data in the broad energy range of  $0.5 - 150$  keV during the initial phase of the 2015 outburst. We have done spectral analysis with the TCAF model-based *fits* file to extract physical flow parameters. The nature of these model fitted accretion flow parameters allowed us to investigate physical reasons behind origin of the several flares, and their variability and turbulent features. We have also calculated equipartition

The paper is organized in the following way. In Section 2, we will briefly discuss the disk structure prescribed by TCAF and the way flow parameters decide on the spectral shape. In Section 3, we discuss the observations and the data analysis procedure. In Section 4, we present the results of our analysis. In Section 5, we make a discussion based on our result, and finally, in Section 6, we summarize our findings.

## 2 TCAF SOLUTION

TCAF configuration is based on the solution of a set of equations which govern viscous, transonic flows around a black hole (Chakrabarti 1990). In the TCAF solution, an accreting flow has two components: high viscous, high angular momentum, optically thick and geometrically thin Keplerian disk flow ( $\dot{m}_d$ ) which accretes on the equatorial plane; and a weakly viscous, optically thin sub-Keplerian halo component ( $\dot{m}_h$ ) with low angular momentum. The Keplerian disk is immersed within the sub-Keplerian flow. Due to rise in the centrifugal force close to the black hole, the halo matter slows down at the centrifugal barrier and forms an axisymmetric shock (Chakrabarti 1989). The post-shock region or CENBOL is a ‘hot’ and ‘puffed-up.’ region. The Keplerian disk is truncated at the shock location. Multi-colour black body soft photons are generated in the Keplerian disk. A fraction of this soft photons are intercepted by the CENBOL. Depending on the temperature and size of the CENBOL, soft photons become hard photons via inverse-Comptonization at the CENBOL. Conversely, some Comptonized photons reflect from the Keplerian disk and produce a reflection hump. Thus in TCAF, reflection component is self-consistently incorporated. However, a Gaussian line may be required to add if an iron line is present. CENBOL is also considered to be the base of the jets or outflows (Chakrabarti 1999). Toroidal magnetic flux tubes are responsible for the collimation of jet (Chakrabarti & D’Silva 1994; D’Silva & Chakrabarti 1994). Oscillation of CENBOL can be triggered when the cooling and heating times inside CENBOL are similar and the emerging photons produce the quasi periodic oscillations (QPOs) (Molteni et al. 2016; Ryu et al. 1997; Chakrabarti et al. 2015); hereafter C15).

Transient BHCs generally show different spectral states during their outbursts. In TCAF, these observed spectral states are controlled by the flow parameters (two types of accretion rates and two shock parameters). A typical outbursting BHC generally goes through spectral state transitions to form a hysteresis loop as follows: hard state (HS)  $\rightarrow$  hard-intermediate state (HIMS)  $\rightarrow$  soft-intermediate state (SIMS)  $\rightarrow$  soft state (SS)  $\rightarrow$  soft-intermediate state (SIMS)  $\rightarrow$  hard-intermediate state (HIMS)  $\rightarrow$  hard state (HS) (Remillard & McClintock 2006; Nandi et al. 2012; Debnath et al. 2015a). In the upper panel of Fig. 1 (adopted from (Chakrabarti 2018)), we show a cartoon diagram of the above four spectral states under the TCAF paradigm. In the lower panel, typical spectra of each spectral states correspond to the diagrams are shown. In the cartoon diagrams, brown, light green, dark green and grey region represent Keplerian disk, sub-Keplerian halo, CENBOL and jet, respectively.

Due to lower viscosity and angular momentum, the sub-Keplerian matter moves in with free-fall velocity, whereas the Keplerian flow moves in viscous time. When an outburst is triggered, the sub-Keplerian flow dominates in the accretion process since it moves faster than the Keplerian disk. The Keplerian disk is truncated very far away by a large CENBOL. A strong shock (higher  $R$ ) is formed at hundreds of Schwarzschild

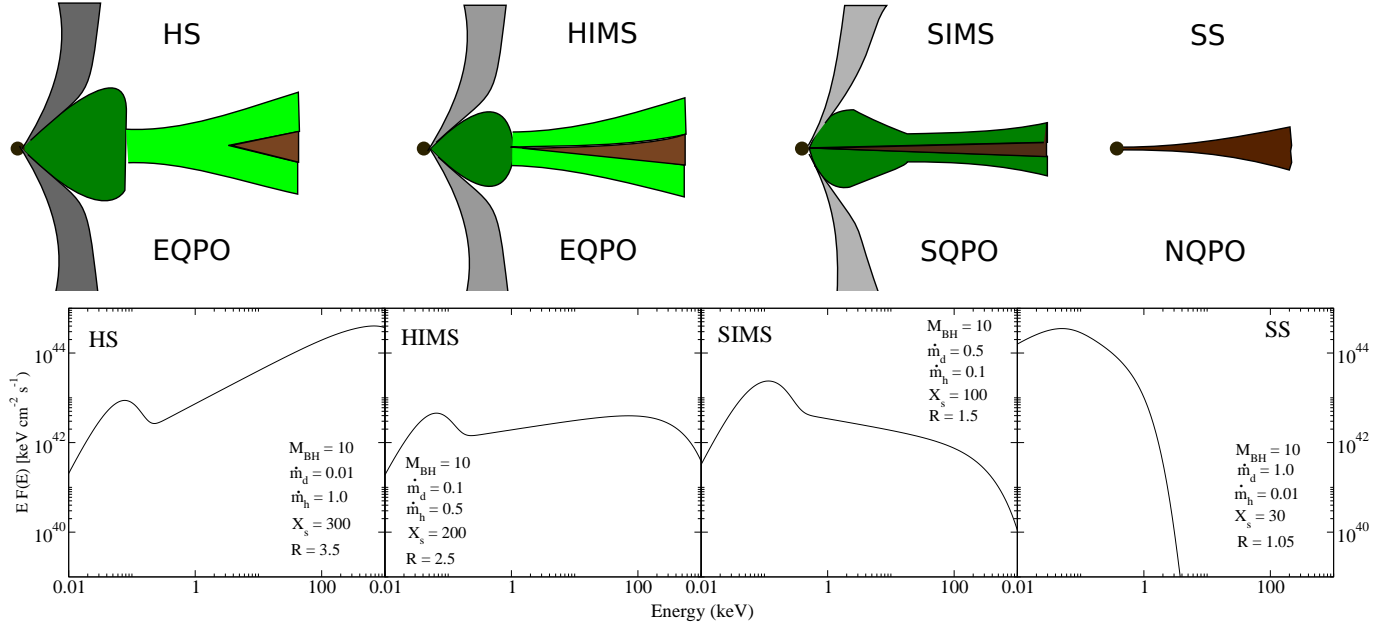


Fig. 1: In upper panel, cartoon diagrams of four commonly observed spectral states under TCAF paradigm are shown (adopted from Chakrabarti 2017). Brown, light green, dark green and grey region represent Keplerian disk, sub-Keplerian halo, CENBOL and jet respectively. An outbursting black hole evolves as  $HS \rightarrow HIMS \rightarrow SIMS \rightarrow SS \rightarrow SIMS \rightarrow HIMS \rightarrow HS$ . Generally both rising and declining HS & HIMS show monotonically evolving type-C (low frequency) QPOs, and SIMS shows sporadic type-B or type-A QPOs due to shock oscillation. In soft state these QPOs are absent, since CENBOL is absent. Here, EQPO means evolving QPO; SQPO means sporadic QPO; NQPO means no QPO. In the bottom panel, theoretical spectra corresponding to the top paneled spectral states are shown. These spectra are generated using five input parameters ( $M_{BH}$  in  $M_{\odot}$ ;  $\dot{m}_d$  in  $\dot{M}_{Edd}$ ;  $\dot{m}_h$  in  $\dot{M}_{Edd}$ ;  $X_s$  in  $r_s$ ,  $R$ ), whose values are marked inset.

X-ray flux dominates and hard state is observed. Compact jet is launched in this state from the CENBOL (Chakrabarti 1999). Evolving type-C QPO is produced in this state due to the resonance oscillation of the shock (Molteni et al. 2016).

The source enters in the HIMS after HS (Fig. 1b). The Keplerian disk accretion rate continues to rise and becomes comparable with the sub-Keplerian halo accretion rate. As a result, accretion rate ratio ( $ARR = \dot{m}_h/\dot{m}_d$ ) decrease. Due to rise of the Keplerian disk accretion rate, CENBOL becomes cooler, and the shock moves farther inward and the CENBOL shrinks. Shock strength decreases as the Compton cooling reduces the post-shock thermal pressure. Mass outflow rate to inflow rate ratio becomes maximum. Here also type-C QPOs are observed.

In the SIMS (Fig. 1c), the Keplerian rate keeps on increasing, although the sub-Keplerian flow rate started to decrease. This is because more and more sub-Keplerian flow becomes Keplerian by viscous transport. The shock becomes weak in this state. The shock further moves in, and the CENBOL becomes small. The soft X-ray flux increases and the hard X-ray flux decreases in this state due to rapid rise in  $\dot{m}_d$  and slow decrease in  $\dot{m}_h$ . Generally, type-A or type-B QPOs are observed sporadically in this state due to weak oscillation of the CENBOL (type-B) or due to oscillation of shock-less centrifugal barrier (type-A).

between  $\dot{m}_h$  and  $\dot{m}_d$  peaks gives us rough estimation of the viscous time scale of the source (Jana et al. 2016). In the SS (Fig. 1d), the Keplerian disk dominates and completely cools down the CENBOL. Soft X-ray flux dominates over hard X-ray flux. No shock is formed. As a result, the jet is completely quenched in this state (Chakrabarti 1999, Garain et al. 2012). No QPO is produced in the soft state.

The flow parameters evolve oppositely during the declining phase of the outburst. Starting from SS to SIMS transition day, both the Keplerian disk accretion rate and the sub-Keplerian halo accretion rate decreases, although, the Keplerian disk rate decreases faster. As a result, ARR increases. As in the SIMS of the rising phase, one may see sporadic type-B or ‘A’ QPOs in the declining SIMS. In the declining HIMS and HS, evolving type-C QPOs could be seen. Similar to the rising phase, one could observe compact jet in the HIMS and HS in the declining phase.

TCAF solution is implemented in XSPEC (Arnaud 1996) to analyze spectral properties around the black holes (Debnath et al. 2014; Debnath et al. 2015a) as an additive table model. TCAF model has input parameters ( $M_{BH}$ ,  $\dot{m}_d$ ,  $\dot{m}_h$ ,  $X_s$ ,  $R$ ). Accretion flow dynamics around several black holes are studied quite successfully using TCAF model (Debnath et al. 2015b; Debnath et al. 2017; Debnath et al. 2020; Jana et al. 2016; Jana et al. 2020b; Chatterjee et al. 2016; Chatterjee et al. 2019; Chatterjee et al. 2020; Bhattacharjee et al. 2017; Shang et al. 2019). Frequencies of the dominating QPOs are predicted from TCAF model fitted shock parameters (Chatterjee et al. 2016). Masses of the black holes are estimated quite successfully from spectral analysis with the TCAF model (Molla et al. 2016; Chatterjee et al. 2016). Jet contribution in the X-rays are also calculated using TCAF solution (Jana et al. 2017; Jana et al. 2020a; Chatterjee et al. 2019).

### 3 OBSERVATION AND DATA ANALYSIS

We analyzed *Swift* data for 19 observations between 2015 June 15 (MJD=57188.77) and June 26 (MJD=57199.52). We studied the source in 0.5 – 150 keV energy band with combined XRT and BAT data for five observations (MJD = 57191.01, 57194.54, 57197.21, 57197.33, and 57198.02). The 15 – 150 keV BAT data was used for four observations (MJD = 57188.77, 57193.56, 57198.15 and 57199.52) when only BAT observations were available. For the rest of the ten observations, we studied 0.5 – 10.0 keV using XRT data.

We used WT mode data for XRT observation. Cleaned event files were generated for XRT using `xrtpipeline` command. To reduce pileup effects, we used grade-0 data. For pileup correction, we chose an annular region around the source. We chose an outer radius of 30 pixels and a varying inner region, depending on the count rate. A background region is chosen far away from the source with 30 pixels radius. Then, we obtained `.pha` and `background` files using these cleaned event files in XSELECT v2.4. A scaling factor was applied to the source and background with BACKSCAL. Spectral data were re-binned to 20 counts per bin using `grppha` command. 0.5 – 10 keV 0.01 sec lightcurves were generated in XSELECT v2.4 using cleaned source and background event files. We followed standard procedures to generate BAT spectra and lightcurves. Detector plane images (dpi) were generated using the task `batbinevt`. For appropriate detector quality, we used `batdetmask` task. Noisy detectors were found, and a quality map

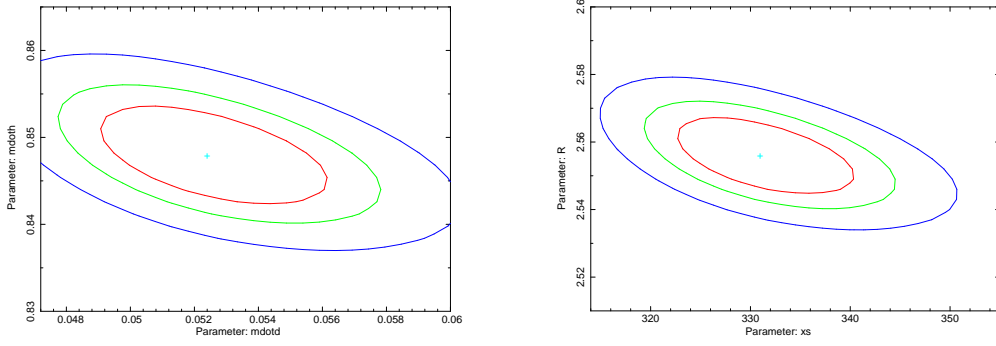


Fig. 2: 2D confidence contour plot for MJD = 57188.77, for (a)  $\dot{m}_d$ - $\dot{m}_h$  and (b)  $X_s$ - $R$ .

mode data. A systematic error was applied to the BAT spectra using `batphasyserr`. Ray-tracing was corrected using `batupdatephakw` task. Then a response matrix for the spectral file was generated using `batdetmask`. BAT lightcurves of 0.01 sec were obtained using `batbinevt` for 15 – 150 keV.

Here, we used the TCAF model-based *fits* file for the spectral analysis. We also used combined ‘diskbb’ (DBB) and ‘powerlaw’ (PL) models to get rough estimation about the thermal and the non-thermal fluxes where a reflection component is often required to find the best fits. TCAF model-based fits do not require any additional component for reflection since the reflection component is already incorporated while generating a spectrum. We required a *Gaussian* model to incorporate  $Fe-k_\alpha$  emission line. We used *phabs* model for interstellar absorption and *pcfabs* model for partial absorption. With the TCAF, we extracted physical parameters such as the mass of the black hole ( $M_{BH}$ ) in solar mass ( $M_\odot$ ), Keplerian disk rate ( $\dot{m}_d$ ) in Eddington rate ( $\dot{M}_{Edd}$ ), sub-Keplerian halo rate ( $\dot{m}_h$ ) in Eddington rate ( $\dot{M}_{Edd}$ ), shock location ( $X_s$ ) (i.e., size of the Compton cloud) in Schwarzschild radius ( $r_s$ ) and the shock compression ratio ( $R = \rho_+/\rho_-$  with  $\rho_+$  and  $\rho_-$  are post- and pre-shock density respectively). In TCAF,  $N$  depends on the distance and inclination angle of the source and is just a constant factor between the emitted flux and observed flux by a given instrument. However, it can vary if any physical processes are present other than the accretion. Since the current version of TCAF model fits file does not include jets, for instance, a variation of normalization is observed if they are present (Jana et al. 2017; Chatterjee et al. 2019). We first analyzed the spectra after keeping the mass of the black hole as a free parameter. We obtained the mass of the black hole in the range of 9.5 – 11.5  $M_\odot$  or average value of 10.6  $M_\odot$ . This measured mass range agrees very well with previously reported values by many authors (Casares et al. 1992; Khargharia et al. 2010). Then, we refitted all the spectra after keeping the mass of the black hole frozen at 10.6  $M_\odot$ . The result based on the later analysis is presented here.

We achieved best-fittings using `steppar` command. After obtaining a best-fit based on  $\chi^2_{red}(\sim 1)$  with TCAF, we ran `steppar` to verify fitted parameter values. The ‘steppar’ command ran for pair of parameters  $\dot{m}_d$ - $\dot{m}_h$  and  $X_s$ - $R$ . We also calculated uncertainties with the `steppar`. In Figs. 2 and 3, 2D-

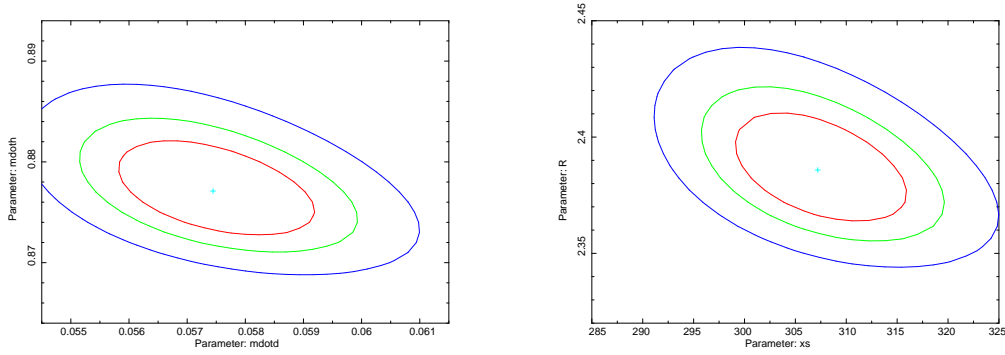


Fig. 3: 2D confidence contour plot for MJD = 57189.62, for (a)  $\dot{m}_d$ - $\dot{m}_h$  and (b)  $X_s$ - $R$ .

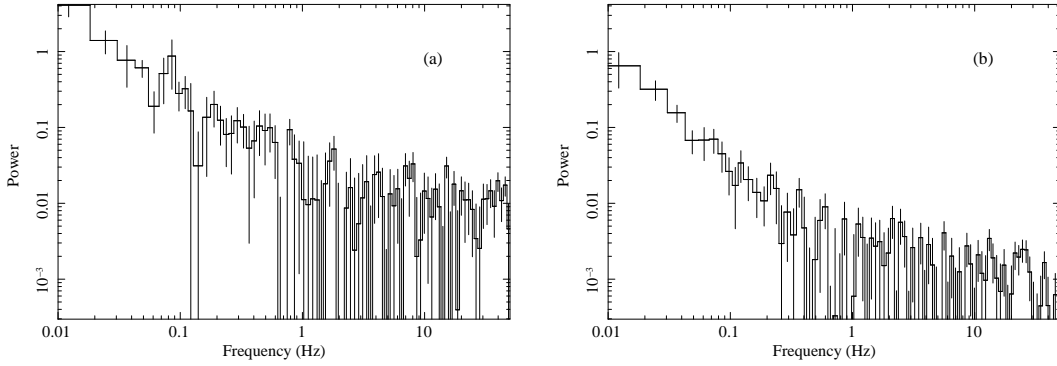


Fig. 4: Power density spectra (PDS) of 0.01 sec time binned lightcurves of 0.5 – 10 keV XRT data. The observation date of these PDS are: 2015 June 18 (MJD = 57191.01) and 2015 June 21 (MJD = 57194.54).

## 4 RESULTS

We present the results of spectral and temporal analysis of the source in 0.5 – 150 keV energy band using combined XRT+BAT or only BAT (in 15 – 150 keV) or only XRT (in 0.5 – 10 keV) data. In Fig. 4, we show two XRT PDS for observation on MJD = 57191.01 (2015 June 18) and MJD = 57194.54 (2015 June 21). In Fig. 5, TCAF model fitted spectrum of combined XRT plus BAT data in the broad energy range 0.5 – 150 keV is shown for the observation on MJD = 57191.01.

In Fig. 6a, we show the evolution of BAT and XRT fluxes. In Fig. 6(b-c), we show the variation of the Keplerian disk rate ( $\dot{m}_d$ ), the sub-Keplerian halo rate ( $\dot{m}_h$ ) with day (in MJD). In Fig. 4d, we show the evolution of accretion rate ratio (ARR =  $\dot{m}_h/\dot{m}_d$ ). In Fig. 7a, we show the variation of the equipartition magnetic field with the day (see, below for details). In Fig. 5(b-d), we show the variation of the shock location ( $X_s$ ), the shock compression ratio ( $R$ ) and TCAF model normalization with the day. In Fig. 8, the time-resolved *Swift*/BAT spectra in the energy range of 15 – 150 keV for the observation on June 15, 2015 (MJD = 57188.77) are shown. The three spectra are marked as (a) (online green), (b) (online black) and (c) (online red) with exposures time of 220 sec, 680 sec and 160 sec, respectively.

### 4.1 Temporal Evolution

The 2015 outburst of V404 Cygni is not like any other regular outburst of transient BHCs. It showed

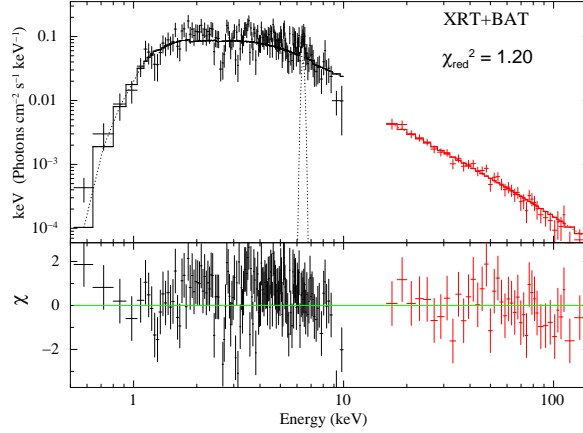


Fig. 5: TCAF model fitted combined XRT+BAT spectra in the energy range of 0.5 – 150 keV, observed on MJD = 57191.03.

minute to hour timescales. Several radio and X-ray flares were observed during this epoch. *INTEGRAL* observation revealed 18 X-ray flares during the outburst (Rodríguez et al. 2015). Radio flare were also reported (Mooley et al. 2015a; Trushkin et al. 2015b; Tetarenko et al. 2017). We find that the luminosities were Eddington or super-Eddington in some observations. On 2015 June 22 (MJD = 57195.41), the XRT flux increased rapidly to  $4.61 \times 10^{-7}$  ergs  $s^{-1}$  from  $8.2 \times 10^{-8}$  ergs  $s^{-1}$  of the previous observation. This corresponds to the source luminosity,  $L \simeq 3.13 \times 10^{38}$  ergs  $sec^{-1}$ . On June 25, 2015 (MJD = 57198.93), the XRT flux reached at  $4.59 \times 10^{-6}$  ergs  $sec^{-1}$  which corresponds to the source luminosity,  $L \simeq 3.12 \times 10^{39}$  ergs  $sec^{-1}$ . BAT count rate also increased rapidly within our analysis period. It became maximum on June 26, 2015 (MJD = 57198.93) at  $4.68 \times 10^{-7}$  ergs  $sec^{-1}$ , *i.e.*, luminosity was  $L \simeq 3.18 \times 10^{38}$  ergs  $sec^{-1}$ .

We studied power density spectra (PDS) of 0.01 sec binned lightcurve of *Swift*/XRT. We did not find any clear evidence of QPOs during the initial phase of the outburst in both XRT and BAT PDS. A weak signature of QPO was observed in the PDS on 2015 June 18 (MJD = 57191.03) (see. Fig 4a). The XRT PDS showed almost flat spectral slope with broad-band noise. The noise decreased as the outburst progressed during which we found two slopes in the PDS, steep powerlaw slope in the lower frequency and flat slope at a higher frequency. In some PDS, we observed that power diminished very rapidly. We did not find any break in the PDS. Similar nature is also observed in BAT PDS.

#### 4.2 Evolution of the Spectral Properties

We have done the spectral analysis using 0.5 – 150 keV combined *Swift*/XRT and *Swift*/BAT data between 2015 June 15 and 26. (Radhika et al. 2016) analyzed the same data set using phenomenological *diskbb* and *powerlaw* models. We analyzed the data with combined *diskbb* and *powerlaw* models and have found similar results as in (Radhika et al. 2016). In general, we used ‘*phabs \* pcf \* (diskbb + powerlaw + gaussian)*’ model to estimate thermal and non-thermal fluxes. While analyzing with phenomenological models, we did not require *diskbb* component on a regular basis. *Diskbb* component was required only in 9 observations out of a total 19 observations. During the entire period, PL photon index varied between 0.60



emission along with the ‘*diskbb + powerlaw*’ model. Detailed results of the phenomenological model are given in Table I.

In the present paper, our main goal is to study the accretion flow dynamics of the source from spectral analysis with the physical TCAF model. For this purpose, we used ‘*phabs \* pcf \* (TCAF + gaussian)*’ model. Detailed results using this model is presented in Table II. From the spectral analysis in the initial few observations, we obtained very low values of the Keplerian disk rate ( $\dot{m}_d$ ) while the sub-Keplerian halo rates ( $\dot{m}_h$ ) were found to be high ( $> 0.85\dot{M}_{Edd}$ ). On 2015 June 19 (MJD = 57192.16),  $\dot{m}_h$  increased to  $1.37\dot{M}_{Edd}$  from its previous day value of  $0.85\dot{M}_{Edd}$ . After that, it varied within  $1.24 - 1.58\dot{M}_{Edd}$  until the end of our analysis period. On 2015 June 25 (MJD = 57198.02), we observed sudden rise in  $\dot{m}_d$  from its previous day, i.e., from  $0.11\dot{M}_{Edd}$  to  $0.15\dot{M}_{Edd}$ . Before that,  $\dot{m}_d$  varied in the range of  $0.05 - 0.12\dot{M}_{Edd}$ . After MJD = 57198.02,  $\dot{m}_d$  was obtained in a narrow range of  $0.13 - 0.16\dot{M}_{Edd}$  (see Fig. 6b).

A strong shock ( $R = 2.56$ ) was found far away from the black hole ( $X_s = 334 r_s$ ) on the first day (MJD=57188.77) of our observation (see Fig. 7b & 7c). The shock remained strong for the next five days. After that, the shock was found to move closer to the black hole as the Keplerian disk rate increased. The shock was found at  $126 r_s$  on MJD = 57194.16 with  $R = 1.92$ . The shock did not move closer than this. After that, shock moved away from the black hole. Again we found that the shock was moving inward after MJD=57197.21. On the last day of our observation, we found the shock to be at  $143 r_s$ .

We add a *Gaussian* profile along with the TCAF solution to incorporate the contribution of the *Fe* emission line in XRT data. Fe-line varied within 6.08 keV and 6.97 keV. In some observation, we required the line width of  $> 1$  keV. We used *phabs* models for the interstellar absorption. We did not freeze  $n_H$  at a particular value. Rather, we kept it free. In our analysis, we observed it to vary between  $0.54 \times 10^{22}$  to  $1.49 \times 10^{22} \text{ cm}^{-2}$ . We also used *pcfabs* model to incorporate for partial absorption in XRT data. In some observations, the covering required as high as 95%. In general, it varied between 50% and 95%. For covering absorption,  $n_H$  varied between  $2.2 \times 10^{22}$  and  $28.9 \times 10^{22} \text{ cm}^{-2}$ .

### 4.3 Time Resolved BAT Spectra

To study the evolution of spectral nature in short time intervals, we analyzed the time-resolved BAT spectra. Rapid variation of the accretion rates and other physical flow parameters from observation to observation motivated us to make this study. Here, we analyzed time-resolved BAT spectra for four observations on June 15, 2015 (MJD = 57188.77), June 18, 2015 (MJD = 57191.03), June 20, 2015 (MJD = 57193.56) and June 26, 2015 (MJD = 57199.52). We found rapid variation in the BAT spectra within very short period of time even in one observation. In Table III, TCAF model fitted parameters for time-resolved spectra are presented. For example, on 2015 June 15, within total BAT exposure of 1202 sec (Fig. 8), we observed the variations of  $\dot{m}_d$  between 0.041 and  $0.057\dot{M}_{Edd}$ , and  $\dot{m}_h$  between 0.82 and  $0.88\dot{M}_{Edd}$ . The shock was observed to vary in between  $\sim 326 - 336 r_s$ . Similar rapid variation of the flow parameters ( $\dot{m}_d$  &  $\dot{m}_h$ )

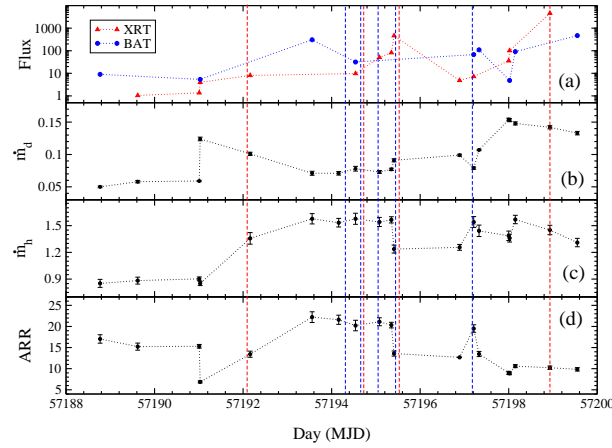


Fig. 6: Panel (a) shows variation of 0.5 – 10 keV XRT and 15 – 150 keV BAT flux with day (MJD). The red (online) triangle represents XRT flux while blue (online) circle represents BAT flux. The fluxes are in the unit of  $10^{-9} \text{ ergs/sec}$ . The variation of (b)  $\dot{m}_d$  in  $\dot{M}_{Edd}$  and (c)  $\dot{m}_h$  in  $\dot{M}_{Edd}$  are shown with day (MJD). In panel (d) the variation of ARR ( $=\dot{m}_h/\dot{m}_d$ ) is shown. Blue and red dotted lines represent reported X-ray and Radio flaring activities respectively.

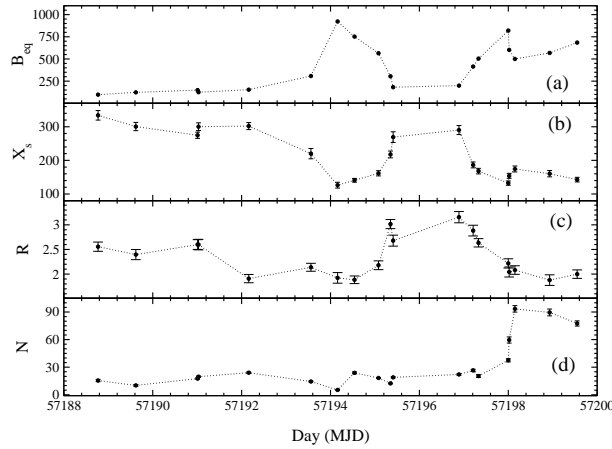


Fig. 7: The variation (a) equipartition magnetic field ( $B_{eq}$ ) in *Gauss*, (b) shock location ( $X_s$ ) in  $r_s$ , (c) shock compression ratio ( $R$ ) and (d) normalization ( $N$ ) are shown with day (MJD).

#### 4.4 Estimation of Magnetic Field

Observation of presence of high magnetic field on 2015 June 25 by (Dallilar et al. 2017) motivated us to estimate magnetic field strength at the ‘hot’ Compton cloud region (here CENBOL) for the BHC V404 Cygni during its 2015 outburst. We made some simple assumptions as mentioned below to calculate the equipartition value of the magnetic field. At the shock location, energy conservation leads to the following equation (Chakrabarti 1990),

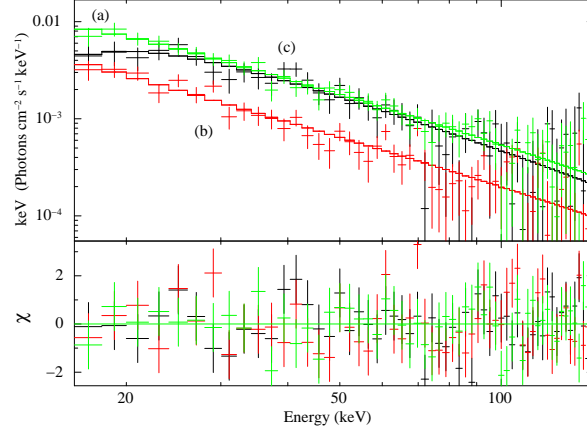


Fig. 8: Time resolved BAT spectra for observation on MJD = 57188.77 is shown. The spectra correspond to exposures of (a) 220 sec, (b) 680 sec and (c) 160 sec.

where,  $n$  is the polytropic index of the flow,  $a$  is sound speed,  $V$  is particle velocity. ‘+’ and ‘-’ signs indicate the values at post- and pre-shock region respectively. The electron number density ( $n_e$ ) is given by,

$$n_e = \frac{\dot{m}_d + \dot{m}_h}{4\pi X_s V_+ H_{shk} m_p}. \quad (2)$$

For our calculation, we assume CENBOL shape as cylindrical.  $m_p$  is the mass of the proton.  $H_{shk}$  is the shock height. The shock height could be calculated from the TCAF model fitted shock parameters (Debnath et al. 2015a) using standard vertical equilibrium (Chakrabarti 1989),

$$H_{shk} = \sqrt{\frac{n(R-1)X_s^2}{R^2}}. \quad (3)$$

Now, we can calculate pressure at CENBOL using the following equation,

$$P_{gas} = \frac{a_+^2 m_e n_e}{n}. \quad (4)$$

We consider equipartition magnetic field ( $B$ ) as,

$$\frac{B^2}{8\pi} = P_{rad} + P_{gas}, \quad (5)$$

where,  $P_{rad}$  is the radiation pressure. The radiation pressure is negligible compared to the gas pressure. Using this equation, we calculated the maximum possible value of the equipartition magnetic field for this source (see, Table IV). We show the variation of the equipartition magnetic field in Fig. 7a. We find  $B = 97 G$  on our first observation (MJD = 57188.77). Then we found that  $B$  was increasing with the shock moving towards the black hole.  $B$  was maximum on 2015 June 21 (MJD = 57194.16) at 923  $G$ . On that day, the shock was closest to the black hole.

#### 4.5 Cooling Time

V404 Cygni did not show any strong QPO during its 2015 outburst. Although there are numerous suggestions for the origin of low frequency QPOs, we believe that these QPOs are generated due to the oscillation of the shock formed in TCAF solution. This shock oscillates when the resonance condition between cooling

shock (Molteni et al. 2016; Ryu et al. 1997; Chakrabarti et al. 2015). Thus to check if the resonance condition is satisfied or not, we have calculated both cooling and infall time scales during the outburst. Generally in low mass X-ray binaries, Compton cooling is the primary process of cooling. We also considered the synchrotron cooling since the magnetic field was present.

We calculated both cooling time scales (synchrotron and Compton) during the entire period of our observations and compared that with the infall times. If cooling and infall timescales are roughly comparable, then we may say that the resonance condition for oscillation of the shock is satisfied. For simplicity, here we assume that the matter is moving radially at the post-shock region with speed  $V_+$ . This allowed us to calculate infall time using the following equation,

$$t_{inf} = \frac{X_s}{v_+} \quad (6)$$

Similar to the magnetic field calculation, here we also assume CENBOL as a cylindrical in shape. Now the total thermal energy of electron content within the CENBOL is,

$$E = \gamma_e m_e c^2 V n_e, \quad (7)$$

where  $\gamma_e$  is the Lorentz factor. It is given by,  $\gamma_e = 1/\sqrt{1 - \beta_e^2}$ , where  $\beta_e = v/c$ ,  $v$  being electron velocity and  $c$  is the velocity of light. The synchrotron cooling rate is (Rybicki & Lightman 1979),

$$\Lambda_{syn} = \frac{4}{3} \sigma_T c \beta_e \gamma_e^2 U_B, \quad (8)$$

where  $\sigma_T$  is Boltzman constant.  $U_B$  is magnetic energy density and given by,  $U_B = B^2/8\pi$ . The synchrotron cooling time is given by,

$$t_{syn} = \frac{E}{\Lambda_{syn}}. \quad (9)$$

We calculated cooling time due to synchrotron using Eqn. 9. Note, we use  $\gamma_e=10$  for our calculation. We also checked the Compton cooling timescale ( $t_{Comp}$ ). To calculate Compton cooling, we use the same method as described in C15. The Compton cooling timescale is given by Eqn. 6 of C15,

$$t_{Comp} = \frac{E}{\Lambda_{Comp}}. \quad (10)$$

Here,  $\Lambda_{Comp}$  is Compton cooling rate (for more details, see, C15). Here we find that the Compton cooling is much faster than the synchrotron cooling (see, Table IV). Thus we may assume that inverse-Comptonization is the primary process for cooling. Now if we compare  $t_{inf}$  with  $t_{syn}$  or with  $t_{Comp}$ , in both the cases, the ratio deviates largely from unity. Thus we may say that during the 2015 outburst of V404 Cygni, resonance conditions are not satisfied to form oscillating shock. This indeed verifies the observational fact of the no prominent signature of type-C low frequency QPOs during the outburst. The detailed results of our calculation of the magnetic field and two types of cooling time scales are presented

## 5 DISCUSSION

*Swift*/XRT and BAT data for 19 observations between 2015 June 15 (MJD=57188.77) and June 26 (MJD=57199.52) are used to study properties of the V404 Cygni in a broad energy range of 0.5 – 150 keV. The TCAF model fitted spectral analysis allowed us to understand the nature of this violent outburst from a physical perspective. The source exhibited this outburst after a long 26 years of quiescent. During this outburst, many radio and X-ray flares were also observed. The presence of a strong magnetic field is considered to be one of the reasons behind this unusual outburst of V404 Cygni. In the following sub-Sections, we discuss those in details.

### 5.1 Magnetic Field

A magnetic field is brought in by the accretion flow. The shear, convection and advection amplify the predominantly toroidal flux tubes. They are expelled from the CENBOL due to the magnetic buoyancy (Chakrabarti & D'Silva 1994; D'Silva & Chakrabarti 1994) in the direction towards the pressure gradient force. If the buoyancy timescale is larger than the shear amplification timescale, then the magnetic flux tubes are amplified within the dynamical timescale until they reach equipartition where gas pressure matches with the magnetic pressure. In general, the magnetic field is not found to contribute to the accretion disk spectra of black holes since TCAF alone fits the data very well. However, it is necessary for acceleration and collimation of jets and outflow.

Here, we calculated the equipartition magnetic field by equating magnetic pressure with the local gas pressure at the shock. We found  $B_{eq} = 97 G$  on the first observation day. After that, it increased gradually with the increase of the accretion rate. We found the maximum value of the magnetic field to be  $B_{eq} = 923 G$  on June 21, 2015 (MJD = 57194.16). Then, it decreased to 154 G on MJD = 57196.89. Then, we observed that it was varying between 414 and 820 G within our observation. Dallilar et al. calculated the equipartition magnetic field for this source to be  $461 \pm 12 G$  on June 25, 2015 (MJD = 57198.18) (Dallilar et al. 2017). We found it  $B_{eq} = 500 \pm 18 G$  on that day (MJD = 57198.15). However, our estimated value of the magnetic field is much lower than the previously estimated values for other Galactic black holes. Previously, magnetic field was found to be about  $\sim 10^5 - 10^7 G$  for Cygnus X-1 (Del Santo et al. 2013);  $\sim 5 \times 10^4 G$  for XTE J1550-564 (Chatty et al. 2011); and  $\sim 1.5 \times 10^4 G$  for GX 339-4 (Cutri et al. 2003). However, the magnetic field was calculated in a jet for these sources; thus, they showed much higher values.

### 5.2 Power Density Spectra

No prominent QPOs were observed in the PDS of the Fourier transformed 0.01 sec time binned XRT lightcurves in the 0.5 – 10 keV energy band. Presence of a significant magnetic field may cause turbulence in the accretion disk, which could be responsible for the white noise observed in the PDS. The PDSs were observed to have two slopes: a powerlaw component and a flat component. Powerlaw slope was observed in the lower frequency region while flat slope was observed in the higher frequency. The turbulence could be the reason behind the flat spectrum observed in the XRT PDS. Power in the PDS follows as,  $P \sim 1/f^\beta$ , where  $f$  is the frequency and  $\beta$  is powerlaw index. In the most PDS, we found  $\beta \sim 0$ , *i.e.*, flat spectra. It

This also indicates no or minimal contribution of the Keplerian disk accretion. Precisely, this is found from the spectral analysis.

### 5.3 Absence of QPOs

We believe that the oscillation of shock is responsible for the QPOs (Molteni et al. 2016). Generally strong type-C QPOs are observed if the resonance condition is satisfied, i.e., when the infall time of the post-shock matter roughly matches with the cooling time inside the CENBOL. The shock oscillation could also be observed when Rankine-Hugoniot conditions are not satisfied to form a stable shock (Ryu et al. 1997). According to C15, the type-B or type-A QPOs mainly occur due to weak resonance phenomenon in CENBOL (type-B) or in shock-less centrifugal barrier (type-A). The cooling process could be via inverse-Compton scattering, bremsstrahlung or synchrotron emission. If the magnetic field is high enough, one can expect the dominance of synchrotron cooling.

We did not observe any prominent type-C QPOs during the 2015 outburst of V404 Cygni. Non-satisfaction of the resonance condition could be responsible for it. To verify this assertion, we calculated synchrotron and Compton cooling times for this source. We found that the Compton cooling rate is much faster than the synchrotron cooling rate. Thus Compton cooling dominated the cooling process. We compared both types of cooling times with the infall time. We found that the infall time and cooling time were not comparable at all (see Table IV). C15 showed that QPO would be generated if the ratio of the infall and the cooling times is between 0.5 and 1.5, i.e., within 50% of unity either way. Since the resonance condition was not satisfied, we were not supposed to see any strong type-C QPOs.

Huppenkothen et al. 2017 reported of detection of mHz QPO with *Chandra*, *Swift*/XRT and *Fermi* observations (Huppenkothen et al. 2017). They reported simultaneous detection of 18 mHz QPO with *Swift*/XRT and *Fermi*/GBM. They classified this QPO as a new type of low-frequency QPO. However, Radhika et al. argued that they did not find any clear signature of this QPO (Radhika et al. 2016). *Chandra*/ACIS observation revealed signatures of 73 mHz and 1.03 Hz QPOs. However, they did not seem to be type-C QPOs. Thus the resonance condition was not behind the origin of these QPOs. This could be due to non-satisfaction of the Rankine-Hugoniot conditions at the shock front.

### 5.4 Spectral and Temporal Evolution

V404 Cygni showed complex behaviour during the 2015 outburst. We required two absorption models to fit the spectra: *phabs* model for interstellar absorption and *pcfabs* for the partial covering absorption. The later absorption may be due to disk wind emission or outflow emission (King et al. 2015; Radhika et al. 2016). Variable dust scattering rings were observed with XRT (Beardmore et al. 2015; Vasilopoulos et al. 2016). After MJD = 57198, the dust halo started to dominate in the field of view; hence we studied the spectral and the timing properties up to this day.

Some observations of V404 Cygni could not be fitted with simple disk blackbody and powerlaw models since a significant reflection component was present. In the first six observations, DBB component was not required to fit the spectra (till MJD = 57193.56). After that, it was required occasionally. PL photon

ing the entire period of our observation. We often observed a ‘hump’ region after  $\sim 8$  keV in the XRT data. This ‘reflection hump’ was extended up to  $\sim 20$  keV in the BAT data. Radhika et al. had also analyzed 0.5 – 150 keV combined XRT+BAT data using disk blackbody (diskbb) and PL models and found similar results (Radhika et al. 2016). Later, they used ‘pexrav’ model instead of ‘PL’ model for this reflection. In their analysis, disk blackbody component was not required in a few observations. They found photon indices varied randomly between 0.60 and 4.43. (Rodriguez et al. 2015; Natalucci et al. 2015) and (Roques et al. 2015) analyzed *INTEGRAL*/IBIS and *INTEGRAL*/SPI data with Comptonization model in the broad energy range of 20 – 650 keV. They required an additional cut-off powerlaw in the energy range of 400 – 600 keV. They found that Comptonization temperature was  $\sim 40$  keV with seed photon temperature  $\sim 7$  keV. This is very high for the disk emission. They concluded that this emission could be of different origins, such as synchrotron emission from the jet.

We extracted the physical parameters of the accretion flows from each fit. We first fitted each spectrum by keeping all model input parameters, including the mass of the black hole as free. We found a variation of  $M_{BH}$  in a narrow range of  $9.5 - 11.5 M_{\odot}$  with an average value of  $10.6_{-1.1}^{+0.9} M_{\odot}$ . This estimated mass of V404 Cygni agrees well with other reported values in the range of  $9 - 12 M_{\odot}$  (Casares et al. 1992; Shahbaz et al. 1994; Khargharia et al. 2010). We then re-fitted all the spectra by keeping  $M_{BH}$  frozen at its most probable value ( $= 10.6 M_{\odot}$ ) to extract values of other physical flow parameters during the outburst.

From the variation of the TCAF model fitted flow parameters (i.e., high dominance of  $\dot{m}_h$  over  $\dot{m}_d$  and presence of strong shock ( $R > 2.3$ ) at a large distance), we infer that the source was in the hard state at the beginning of the outburst. High ARR ( $\sim 14 - 22$ ) also indicates this except in one observation made on 2015 June 18 (MJD=57191.03). From the phenomenological model fittings, the dominance of powerlaw flux also indicates this. On 2015 June 25 (MJD=57198), we observed that  $\dot{m}_d$  started to increase rapidly although other parameters did not change much, leading to softening of the spectra. At this last phase of our observation, we observed that ARR was decreasing with an increase in the Keplerian disk rate. During this phase, the source may be in the hard-intermediate state. In general, spectral state classification is done based on the variation of ARR and the nature of QPO. Due to the absence of QPOs and complex behaviour of the ARR, we have not been able to assert the exact state transition day but the source likely entered in the hard-intermediate state on MJD = 57197.21 when  $\dot{m}_h$  was found to achieve its maximum rate. After this day,  $\dot{m}_d$  was found to increase rapidly. However, our classification may not be valid since the source showed rapid fluctuation in very short timescale (Motta et al. 2017). Motta et al. analyzed the time-resolved *Swift*/XRT spectra and found that spectra shape changed in as short as  $\sim 10$  sec (Motta et al. 2017).

The 2015 outburst is somewhat similar to the 2003 outburst of H 1743-322. Both outbursts occurred after long quiescence periods. Like the 2015 outburst of V404 Cygni, the 2003 outburst of H 1743-322, which also occurred after about 26 years, showed peculiar behaviour with several flares and outflow activity. Thus it is possible that a huge amount of matter accumulated at a large pileup distance over a long time. With a sudden enhancement of viscosity, the outburst is triggered and leads to a violent and non-settling activity

## 5.5 Evolution of the Spectral Properties with Flares

The present outburst of V404 Cygni did not behave like any other typical outburst of a classical transient black hole. V404 Cygni showed a strong jet associated with several flares. The flares were observed in multi-wavebands, from X-ray, optical, IR to radio (Rodriguez et al. 2015; Gandhi et al. 2016; Trushkin et al. 2015a; Trushkin et al. 2015b; Tetarenko et al. 2017). Eighteen X-ray flares were reported with the *INTEGRAL* and *SWIFT*/BAT observations between June 20, 2015 (MJD = 57193) and June 25, 2015 (MJD = 57198). The magnetic field was the strongest during this phase of the outburst. The magnetic field could be responsible for this flaring activity.

In general, we see a decreasing ARR in an observation immediately after a flare, indicating softening of the spectra (see Fig. 6). For example, an X-ray flare was observed on MJD = 57194.31 (Rodriguez et al. 2015). This could be due to the high magnetic field on MJD = 57194.16. Immediately after the flare, on MJD = 57194.54, we found that the ARR decreased slightly from its previous observation (21.6 to 20.2). On June 18, 2015 (MJD = 57191) we observed that the Keplerian disk rate suddenly rose to  $0.12 \dot{M}_{Edd}$  from  $0.06 \dot{M}_{Edd}$  within  $\sim 30$  mins. This could be associated with the radio flare observed on MJD = 57191.09 with AMI-LA observation (Mooley et al. 2015a). This is expected since a large amount of mass was ejected from the CENBOL during a flare and inflowing matter rapidly moved inward to fill the vacant space. This led to the softening of the spectrum as the CENBOL size was reduced. However, this was not observed after every flare. It is possible that those flares were not localized and the disk was unstable. Around MJD = 57198, we found that  $B_{eq}$  decreased sharply, although  $N$  increased very rapidly. This could be due to the high magnetic field which produced flare and outflow. This flare and the outflow was responsible for the rapid rise of  $N$ .

The X-ray jet flux can be calculated based on the deviation of the constancy of the TCAF model normalization (Jana et al. 2017; Jana et al. 2020a; Chatterjee et al. 2019). However, to calculate jet X-ray flux by this model, we must have at least one observation where the effects of the jet were negligible. In that observation, the entire observed X-ray should be contributed only from the inflowing matter of the accretion disk and CENBOL. However, for V404 Cygni, a strong jet was present in all the observations. Thus we were not able to separate the jet X-ray contribution from the total X-ray. Random variation in normalization may be due to the presence of fluctuating magnetic field or unsettling disk, which led to the flaring activity of the source.

## 6 SUMMARY

The first epoch of the 2015 outburst of the Galactic black hole V404 Cygni was an unusual and violent outburst. It did not behave like other typical outbursts of Galactic transient black hole candidates. Rapid variations were observed in both spectral and timing properties in a very short time scales, ranging from a few minutes to hours. We have used 0.5 – 150 keV combined *Swift*/XRT and *Swift*/BAT data to study the accretion flow properties of the source. Spectral analysis was done using the TCAF model-based *fits* file in XSPEC. The model fitted/derived flow parameters allowed us to understand the evolution of accretion flow parameters of this violent outburst. We have also calculated the equipartition magnetic field for the outburst.



This is also confirmed from the spectral analysis. The presence of white noise in higher frequencies in the power density spectra indicates the presence of a highly turbulent disk. The strong magnetic field could be the reason behind it. It is also responsible for the flares. We find that the Compton cooling process is much faster than the synchrotron cooling process. Since the resonance condition between cooling and infall time scales inside the CENBOL is not satisfied, we did not expect any sharp low frequency QPO. Indeed the object did not show any signature of prominent type-C QPO.

**Acknowledgements** This work made use of XRT and BAT data supplied by the UK *Swift* Science Data Centre at the University of Leicester. We acknowledge anonymous referee for his kind suggestion to improve the quality of the paper. A.J. and D.D. acknowledge support from DST/GITA sponsored India-Taiwan collaborative project (GITA/DST/TWN/P-76/2017) fund. A.J. also acknowledges CSIR SRF fellowship (09/904(0012) 2K18 EMR-1). Research of D.D. and S.K.C. is supported in part by the Higher Education Dept. of the Govt. of West Bengal, India. D.D. also acknowledges the ISRO sponsored RESPOND project (ISRO/RES/2/418/17-18) fund. D.C. and D.D. acknowledge support from DST/SERB sponsored Extra Mural Research project (EMR/2016/003918) fund. J.-R. S., and H.-K. C. are supported by MOST of Taiwan under grants MOST/106-2923-M-007-002-MY3 and MOST/107-2119-M-007-012.

## References

- Arnaud, K.A., 1996, ASP Conf. Ser., Astronomical Data Analysis Software and Systems V, ed. G.H. Jacoby & J. Barnes, 101, 17
- Barthelmy S. D., DAi A., DAvanzo P., Krimm H. A., Lien A. Y., Marshall F. E., Maselli A., Siegel M. H., 2015, GCN Circ., 17929
- Beardmore A. P., Altamirano D., & Kuulkers E., et al. 2015, ATel, 736, 1
- Bhattacharjee, A., Banerjee, I., & Banerjee, A., et al. 2017, MNRAS, 466, 1372
- Casares J., Charles P. A., Naylor T., 1992, Nature, 355, 614
- Chakrabarti, S. K., 1989, MNRAS, 240, 7
- Chakrabarti, S. K. 1990, Theory of Transonic Astrophysical Flows (Singapore: World Scientific)
- Chakrabarti, S. K.; Molteni, D., 1993, ApJ, 417, 671
- Chakrabarti, S. K., & D'Silva, S. 1994, ApJ, 424, 138
- Chakrabarti, S.K., 1995, in Ann. NY Acad. Sci., Seventeenth Texas Symposium on Relativistic Astrophysics and Cosmology, eds. H. Bohringer, G.E. Morfil and J. Trumper, 546.
- Chakrabarti, S. K., & Titarchuk, L.G., 1995, ApJ, 455, 623
- Chakrabarti, S.K., 1997, ApJ, 484, 313
- Chakrabarti, S. K., 1999, A&A, 351, 185
- Chakrabarti, S. K., Mondal, S., & Debnath, D., 2015, MNRAS, 452, 3451
- Chakrabarti, S. K., 2018, MG14 Conf. Pro., World Scientific Press, Singapore, Edited by, R. Ruffini, R. Jantzen, M. Bianchi, 369
- Chakrabarti, S. K., Nagarkoti, S., & Debnath, D., 2019, AdSpR, 63, 3749
- Chatterjee, D., Debnath, D., Chakrabarti, S. K., et al. 2016, ApJ, 827, 88

- Chatterjee, K., Debnath, D., & Chatterjee, D., et al., 2020, MNRAS, 493, 2452
- Chaty, S., Dubus, G., & Raichoor, A., 2011, A&A, 529, 3
- Cutri, R. M., Skrutskie, M. F., & van Dyk, S., et al. 2003, VizieR Online Data Catalog. no. 2246
- Dallilar, Y., Eikenberry, S. S., & Garner, A., et al. 2017, Sci, 358, 1299
- Debnath, D., Mondal, S., & Chakrabarti, S. K., 2014, MNRAS, 440, L121
- Debnath, D., Mondal, S., & Chakrabarti, S. K., 2015a, MNRAS, 447, 1984
- Debnath, D., Molla, A.A., Chakrabarti, S.K., & Mondal, S., 2015b, ApJ, 803, 59
- Debnath, D., Jana, A., Chakrabarti, S. K., & Chatterjee, D., 2017, ApJ, 850, 92
- Debnath, D., Chatterjee, D. Jana, A., Chakrabarti, S. K., & Chatterjee, K., 2020, RAA (in press)
- Del Santo, M., Malzac, J., & Belmont, R., et al. MNRAS, 430, 209
- D'Silva, S., Chakrabarti, S. K., 1994, ApJ, 424, 149
- Esin, A. A., McClintock, J. E., Narayan, R., 1997, ApJ, 489, 865
- Gandhi, P., Littlefair, S. P., & Hardy, L. K., et al. 2016, MNRAS, 459, 554
- Garain, S. K., Ghosh, H., & Chakrabarti, S. K., 2012, ApJ, 758, 114
- Gazeas K., Vasilopoulos G., Petropoulou M., & Sapountzis K., 2015, ATel, 7650, 1
- Giri, K., Chakrabarti, S. K., Samanta, M. M., Ryu, D., 2010, MNRAS, 403, 516
- Haardt, F., & Maraschi, L., 1993, ApJ, 413, 507
- Heinz, S., Corrales, L., Smith, R., et al. 2016, ApJ, 825, 15
- Huppenkothen, D., Younes, G., Ingram, A., et al. 2017, ApJ, 834, 90
- Jana, A., Debnath, D., Chakrabarti, S. K., et al. 2016, ApJ, 819, 107
- Jana, A., Chakrabarti, S. K., & Debnath, D., 2017, ApJ, 850, 91 (JCD17)
- Jana, A., Debnath, D., Chakrabarti, S. K., & Chatterjee, D., 2020a, RAA, 20, 28
- Jana, A., Debnath, D., & Chatterjee, D., et al. 2020b, ApJ (in press)
- Jenke P. A., Wilson-Hodge, C. A., & Homan, J., et al., 2016, ApJ, 826, 37
- King A. L., Miller J. M., & Raymond J., et al. 2015, ApJ, 813, L37
- Khargharia J., Froning C. S., Robinson E. L., 2010, ApJ, 716, 1105
- Lipunov, V., Gorbovskoy, E., & Tiurina, N., et al. 2015, Atel, 8453, 1
- Loh, A., Corbel, S., & Dubus, G., et al. 2016, MNRAS, 462, L111
- Makino F., 1989, IAU Circ., 4782, 1
- Miller-Jones J. C. A., Jonker P. G., & Dhawan V., et al. 2009, ApJ, 706, L230
- Molla, A. A., Debnath, D., & Chakrabarti, S. K. et al. 2016, MNRAS, 460. 3163
- Mondal, S., Debnath, D., & Chakrabarti, S.K., 2014, ApJ, 786, 4
- Mondal, S., Chakrabarti, S.K., & Debnath, D., 2016, Ap&SS, 361, 309
- Molteni D., Sponholz H., & Chakrabarti S. K., 1996, ApJ, 457, 805
- Mooley K., Fender R., & Anderson G., et al. 2015a, ATel, 7658, 1
- Mooley K., Clarke F., Fender R., 2015b, ATel, 7714, 1
- Motta, S. E., Kajava, J. J. E., & Sanchez-Fernandez, C., et al. 2017, MNRAS, 471, 1797
- Nandi, A., Debnath, D., Mandal, S., et al. 2012, A&A, 542, 56
- Narayan, R., Yi, I., 1994, ApJ, 428, L13

- Natalucci L., Fiacchi M., Bazzano A., Ubertini P., Roques J.-P., Jourdain E., 2015, *ApJL*, 813, L21
- Negoro, H., Matsumitsu, T., Mihara, T., et al. 2015, *The Astronomer's Telegram* 7646, 1
- Novikov, & Thorne, 1973, *Black Holes*, (Eds.) C. DeWitt & B. DeWitt (Gordon & Breach: New York)
- Radhika, D., Nandi, A., Agrawal, V. K., & Mandal, S., 2016, *MNRAS*, 462, 1834
- Remillard R. A., McClintock J. E., 2006, *ARA&A*, 44, 49
- Ritcher, G. A., 1989,
- Rodriguez, J., Cadolle Bel, M., & Alfonso-Garzn, J., et al. 2015, *A&A*, 581L, 9
- Roques J.-P., Jourdain E., Bazzano A., Fiacchi M., Natalucci L., Ubertini P., 2015, *ApJL*, 813, L22
- Ryu, D., Chakrabarti, S. K., & Molteni, D. 1997, *ApJ*, 474, 378
- Rybicki, G. B., & Lightman, A. P., 1979, *Radiative processes in astrophysics* (Wiley, New York)
- Shahbaz T., Ringwald F. A., & Bunn J. C., et al. 1994, *MNRAS*, 271, L10
- Shakura, N.I., & Sunyaev, R. A., 1973, *A&A*, 24, 337
- Shang, J.R., Debnath, D., & Chatterjee, D., et al., 2019, *ApJ*, 875, 4
- Siegert, T., Diehl, R., & Greiner, J., et al. 2016, *Nature*, 531, 341
- Sivakoff G., Bahramian A., & Altamirano D., et al. 2015, *ATel*, 7763, 1
- Sunyaev, R.A., & Titarchuk, L. G., 1980, *ApJ*, 86, 121
- Sunyaev, R.A., & Titarchuk, L. G., 1985, *A&A*, 143, 374
- Tetarenko A., Sivakoff G. R., & Young K., et al. 2015, *ATel*, 7708, 1
- Tetarenko, A. J., Sivakoff, G. R., Miller-Jones, J. C. A., et al. 2017, *MNRAS*, 469, 3141
- Trushkin S. A., Nizhelskij N. A., & Tsybulev P. G., 2015a, *ATel*, 7667, 1
- Trushkin S. A., Nizhelskij N. A., & Tsybulev P. G., 2015b, *ATel*, 7716, 1
- Tsubono K., Aoki T., & Asuma K., et al. 2015, *ATel*, 7701, 1
- Vasilopoulos G., & Petropoulou M., 2016, *MNRAS*, 455, 4426
- Wachmann, A. A., 1948, *Erg. Astron. Nachr.*, 11, 5
- Walton, D. J., Mooley, K., & King, A. L., et al. 2017, 839, 110
- Zdziarski, A. A., Zycki, Piotr T., Svensson, R., Boldt, E., 1993, *ApJ*, 405, 125

**Table I: DBB+PL Model Fitted Spectral Analysis Results**

Obs ID	Day	XRT exp	BAT exp	XRT Flux*	BAT Flux*	DBB Flux*	PL Flux*	$n_H^1$	$n_H^2$	$CF$	$T_{in}$	$\Gamma$	$\chi^2/dof$
(1)	(2)	(3)	(4)	(5)	(6)	(7)	(8)	(9)	(10)	(11)	(12)	(13)	(14)
00643949000	57188.77	—	1202	—	$9.01^{\pm 0.09}$	—	$9.01^{\pm 0.09}$	$0.94^{\pm 0.07}$	—	—	—	$1.59^{\pm 0.13}$	71/53
00031403035	57189.62	1970	—	$1.04^{\pm 0.04}$	—	—	$1.04^{\pm 0.04}$	$1.12^{\pm 0.09}$	$32.7^{\pm 0.2}$	$0.46^{\pm 0.06}$	—	$1.09^{\pm 0.15}$	714/944
00031403038	57191.01	610	—	$1.36^{\pm 0.06}$	—	—	$1.36^{\pm 0.06}$	$0.91^{\pm 0.09}$	$1.61^{\pm 0.06}$	$0.82^{\pm 0.10}$	—	$0.60^{\pm 0.07}$	1013/946
00644520000	57191.03	217	1202	$3.98^{\pm 0.07}$	$5.37^{\pm 0.08}$	—	$9.35^{\pm 0.15}$	$0.59^{\pm 0.08}$	$10.5^{\pm 0.4}$	$0.73^{\pm 0.12}$	—	$1.83^{\pm 0.18}$	394/250
00031403042	57192.16	1262	—	$8.05^{\pm 0.03}$	—	—	$8.05^{\pm 0.03}$	$1.28^{\pm 0.05}$	$11.7^{\pm 0.6}$	$0.95^{\pm 0.10}$	—	$1.39^{\pm 0.18}$	1339/931
00645176000	57193.56	—	542	—	$306.7^{\pm 2.3}$	—	$306.7^{\pm 2.3}$	$0.51^{\pm 0.03}$	—	—	—	$1.20^{\pm 0.15}$	56/51
00031403048	57194.16	4208	—	$4.89^{\pm 0.08}$	—	$1.42^{\pm 0.03}$	$3.47^{\pm 0.04}$	$0.49^{\pm 0.03}$	—	—	$0.19^{\pm 0.03}$	$1.65^{\pm 0.17}$	970/889
00031403046	57194.54	240	7	$9.77^{\pm 0.10}$	$31.8^{\pm 0.7}$	—	$41.6^{\pm 0.3}$	$0.66^{\pm 0.07}$	—	—	—	$1.07^{\pm 0.19}$	1437/882
00031403045	57195.08	930	—	$50.8^{\pm 1.0}$	—	$24.0^{\pm 0.4}$	$26.7^{\pm 0.6}$	$0.54^{\pm 0.05}$	$5.97^{\pm 0.14}$	$0.88^{\pm 0.12}$	$0.15^{\pm 0.03}$	$0.44^{\pm 0.06}$	1192/928
00031403049	57195.35	2977	—	$82.1^{\pm 1.5}$	—	$16.9^{\pm 1.5}$	$65.2^{\pm 2.2}$	$0.62^{\pm 0.04}$	$0.44^{\pm 0.02}$	$0.69^{\pm 0.07}$	$0.95^{\pm 0.12}$	$0.55^{\pm 0.06}$	1282/702
00031403047	57195.41	1903	—	$461.9^{\pm 3.4}$	—	—	$461.9^{\pm 3.4}$	$0.71^{\pm 0.05}$	—	—	—	$1.25^{\pm 0.14}$	975/713
00031403052	57196.89	275	—	$4.84^{\pm 0.09}$	—	$2.67^{\pm 0.21}$	$2.16^{\pm 0.16}$	$0.75^{\pm 0.08}$	$5.83^{\pm 0.15}$	$0.95^{\pm 0.05}$	$0.24^{\pm 0.07}$	$1.48^{\pm 0.29}$	1061/941
00031403054	57197.21	682	5	$7.21^{\pm 0.15}$	$67.8^{\pm 1.2}$	$1.04^{\pm 0.08}$	$74.0^{\pm 1.1}$	$0.96^{\pm 0.11}$	$29.4^{\pm 1.2}$	$0.77^{\pm 0.11}$	$0.21^{\pm 0.06}$	$1.43^{\pm 0.22}$	1409/979
00031403053	57197.33	1052	518	$7.33^{\pm 0.12}$	$109.7^{\pm 1.5}$	—	$117.0^{\pm 1.5}$	$0.48^{\pm 0.09}$	—	—	—	$2.43^{\pm 0.36}$	1107/998
00031403055	57198.00	1028	—	$35.9^{\pm 0.4}$	—	$19.7^{\pm 0.8}$	$16.2^{\pm 0.8}$	$1.08^{\pm 0.18}$	$0.91^{\pm 0.11}$	$0.61^{\pm 0.09}$	$0.76^{\pm 0.10}$	$1.67^{\pm 0.24}$	1250/926
00031403056	57198.02	818	713	$101.6^{\pm 1.8}$	$4.82^{\pm 0.22}$	$101.6^{\pm 1.8}$	$4.82^{\pm 0.33}$	$0.58^{\pm 0.08}$	$9.15^{\pm 0.81}$	$0.81^{\pm 0.11}$	$0.17^{\pm 0.03}$	$1.76^{\pm 0.31}$	1328/994
00031403057	57198.15	—	745	—	$91.4^{\pm 2.4}$	—	$91.4^{\pm 2.4}$	$1.25^{\pm 0.24}$	—	—	—	$1.67^{\pm 0.25}$	39/50
00031403058	57198.93	1312	—	$4592^{\pm 12}$	—	$1.34^{\pm 0.11}$	$4590^{\pm 12}$	$0.95^{\pm 0.09}$	$0.47^{\pm 0.05}$	$0.86^{\pm 0.09}$	$0.98^{\pm 0.12}$	$1.70^{\pm 0.35}$	1322/928
00646721000	57199.52	—	965	—	$468.9^{\pm 4.1}$	—	$468.9^{\pm 4.1}$	$1.22^{\pm 0.17}$	—	—	$0.58^{\pm 0.08}$	$1.82^{\pm 0.27}$	41/49

In Col. 2, UT dates of the year 2015 are mentioned in dd-mm format. In Cols. 4 & 5, XRT and exposures are mentioned.

In Cols. 6 & 7, XRT (0.5 – 10 keV) and BAT (15 – 150 keV) fluxes are mentioned. In Cols. 8 & 9, model fitted disk blackbody (DBB) and powerlaw (PL) fluxes are mentioned.

All fluxes are in the units of  $10^{-9} \text{ ergs cm}^{-2} \text{ s}^{-1}$

$n_H^1$  and  $n_H^2$  are in the unit of  $10^{22} \text{ cm}^{-2}$ .  $n_H^1$  is Hydrogen column density for interstellar absorption.  $n_H^2$  is Hydrogen column density for partial covering absorption.

The Fe emission line energy and  $\sigma$  are mentioned in Col. 15 & 16.

Best fitted values of  $\chi^2$  and degrees of freedom are mentioned in Col. 17 as  $\chi^2/dof$ .

**Table II: TCAF Model Fitted Spectral Analysis Results**

Obs ID	UT Date	Day	$n_H^1$	$n_H^2$	$CF$	$\dot{m}_d$	$\dot{m}_h$	ARR	$X_S$	$R$	$N$	Fe.Line	LW	$\chi^2/dof$
(1)	(2)	(3)	(4)	(5)	(6)	(7)	(8)	(9)	(10)	(11)	(12)	(13)	(14)	(15)
	(DD-MM)	( $MJD$ )	( $\times 10^{22}$ )	( $\times 10^{22}$ )		( $\dot{M}_{Edd}$ )	( $\dot{M}_{Edd}$ )	( $\dot{m}_h/\dot{m}_d$ )	( $r_s$ )			(keV)	(keV)	
00643949000	15-06	57188.77	$1.49^{+0.17}$	—	—	$0.05^{+0.01}$	$0.85^{+0.04}$	$17.0^{+1.0}$	$334^{\pm 15}$	$2.56^{+0.10}$	$15.5^{+1.2}$	—	—	69/51
00031403035	16-06	57189.62	$1.86^{+0.22}$	$28.8^{+1.8}$	$0.41^{+0.03}$	$0.06^{+0.01}$	$0.88^{+0.04}$	$15.2^{+0.8}$	$305^{\pm 13}$	$2.40^{+0.10}$	$10.2^{+0.9}$	—	—	708/899
00031403038	18-06	57191.01	$0.87^{+0.10}$	$2.2^{+0.1}$	$0.93^{+0.10}$	$0.06^{+0.01}$	$0.90^{+0.03}$	$15.3^{+0.4}$	$275^{+10}$	$2.60^{+0.12}$	$17.6^{+0.8}$	$6.57^{+0.11}$	$0.89^{+0.08}$	929/937
00644520000	18-06	57191.03	$1.27^{+0.14}$	$9.3^{+0.4}$	$0.63^{+0.07}$	$0.12^{+0.02}$	$0.85^{+0.03}$	$6.9^{+0.2}$	$300^{+11}$	$2.59^{+0.12}$	$19.7^{+0.9}$	$6.41^{+0.15}$	$1.10^{+0.17}$	338/281
00031403042	19-06	57192.16	$1.20^{+0.11}$	$12.2^{+0.8}$	$0.91^{+0.04}$	$0.10^{+0.01}$	$1.37^{+0.07}$	$13.4^{+0.7}$	$302^{+12}$	$1.91^{+0.08}$	$24.0^{+1.1}$	$6.44^{+0.15}$	$0.74^{+0.13}$	932/787
00645176000	20-06	57193.56	$0.58^{+0.05}$	—	—	$0.07^{+0.01}$	$1.58^{+0.07}$	$22.2^{+1.2}$	$220^{+14}$	$2.14^{+0.09}$	$14.4^{+0.8}$	—	—	54/49
00031403048	21-06	57194.16	$0.57^{+0.09}$	—	—	$0.07^{+0.01}$	$1.53^{+0.07}$	$21.6^{+1.1}$	$126^{\pm 9}$	$1.92^{+0.11}$	$12.4^{+0.4}$	$6.46^{+0.29}$	$0.45^{+0.04}$	1086/899
00031403046	21-06	57194.54	$0.62^{+0.10}$	—	—	$0.08^{+0.01}$	$1.58^{+0.08}$	$20.2^{+1.2}$	$141^{\pm 7}$	$1.88^{+0.09}$	$23.8^{+1.5}$	$6.39^{+0.24}$	$1.20^{+0.22}$	1399/797
00031403045	22-06	57195.08	$0.55^{+0.07}$	$6.2^{+0.2}$	$0.86^{+0.09}$	$0.07^{+0.01}$	$1.54^{+0.05}$	$21.1^{+0.9}$	$162^{+10}$	$2.18^{+0.11}$	$18.3^{+0.6}$	$6.92^{+0.22}$	$1.40^{+0.15}$	1117/928
00031403049	22-06	57195.35	$0.66^{+0.06}$	$18.0^{+0.3}$	$0.66^{+0.05}$	$0.08^{+0.01}$	$1.57^{+0.05}$	$20.3^{+0.7}$	$217^{+12}$	$3.01^{+0.09}$	$12.3^{+0.5}$	$6.91^{+0.18}$	$1.19^{+0.20}$	1067/707
00031403047	22-06	57195.41	$0.63^{+0.05}$	—	—	$0.09^{+0.01}$	$1.24^{+0.05}$	$13.6^{+0.6}$	$269^{+14}$	$2.68^{+0.12}$	$18.9^{+0.9}$	$6.97^{+0.23}$	$0.86^{+0.11}$	982/709
00031403052	23-06	57196.89	$0.84^{+0.10}$	$5.6^{+0.5}$	$0.95^{+0.15}$	$0.10^{+0.01}$	$1.26^{+0.03}$	$12.7^{+0.3}$	$290^{+11}$	$3.16^{+0.11}$	$22.1^{+0.9}$	$6.45^{+0.21}$	$0.30^{+0.05}$	1001/937
00031403054	24-06	57197.21	$1.10^{+0.14}$	$28.9^{+1.3}$	$0.73^{+0.07}$	$0.08^{+0.01}$	$1.54^{+0.04}$	$19.5^{+0.9}$	$187^{\pm 9}$	$2.88^{+0.10}$	$26.5^{+1.2}$	$6.64^{+0.20}$	$0.61^{+0.14}$	1405/981
00031403053	24-06	57197.33	$0.54^{+0.04}$	—	—	$0.11^{+0.01}$	$1.44^{+0.07}$	$13.4^{+0.6}$	$168^{\pm 7}$	$2.63^{+0.10}$	$20.3^{+1.5}$	$6.55^{+0.18}$	$0.29^{+0.06}$	1213/991
00031403055	25-06	57198.00	$0.85^{+0.07}$	$5.2^{+0.4}$	$0.85^{+0.06}$	$0.15^{+0.01}$	$1.39^{+0.05}$	$9.0^{+0.4}$	$132^{\pm 8}$	$2.22^{+0.09}$	$37.5^{+2.7}$	$6.08^{+0.14}$	$0.96^{+0.13}$	937/727
00031403056	25-06	57198.02	$0.60^{+0.04}$	$8.2^{+0.8}$	$0.81^{+0.06}$	$0.15^{+0.01}$	$1.36^{+0.04}$	$8.9^{+0.3}$	$154^{\pm 7}$	$2.04^{+0.12}$	$59.6^{+3.6}$	$6.30^{+0.19}$	$1.11^{+0.16}$	1303/994
00031403057	25-06	57198.15	$1.20^{+0.11}$	—	—	$0.15^{+0.01}$	$1.57^{+0.06}$	$10.6^{+0.4}$	$174^{+10}$	$2.08^{+0.07}$	$93.4^{+2.9}$	—	—	41/51
00031403058	25-06	57198.93	$0.87^{+0.04}$	$3.9^{+0.5}$	$0.92^{+0.05}$	$0.15^{+0.01}$	$1.45^{+0.05}$	$10.2^{+0.4}$	$160^{\pm 9}$	$1.88^{+0.10}$	$89.5^{+4.5}$	$6.22^{+0.22}$	$0.90^{+0.21}$	1423/943
00646721000	26-06	57199.52	$1.15^{+0.16}$	—	—	$0.13^{+0.02}$	$1.31^{+0.05}$	$9.8^{+0.4}$	$143^{\pm 8}$	$1.99^{+0.09}$	$77.5^{+3.3}$	—	—	36/51

In Col. 2, UT dates of the year 2015 are mentioned in dd-mm format.

$n_H^1$  and  $n_H^2$  are in the unit of  $10^{22} \text{ cm}^{-2}$ .  $n_H^1$  is Hydrogen column density for interstellar absorption.  $n_H^2$  is Hydrogen column density for partial covering absorption.

TCAF model fitted/derived parameters are mentioned in Cols. 7-12. The Fe emission line energy and  $\sigma$  are mentioned in Col. 13 & 14.

Best fitted values of  $\chi^2$  and degrees of freedom are mentioned in Col. 15 as  $\chi^2/dof$ .

Note: Mass of the black hole was kept frozen at  $10.6 M_\odot$  during spectral fitting with the TCAF model fits file.

The average values of 90% confidence  $\pm$  values obtained using `steppar` command in XSPEC, are placed as superscripts of fitted parameter values.

**Table III: Time Resolved BAT Spectra**

Obs ID	Day	Spectra	Exposures	$\dot{m}_d$	$\dot{m}_h$	ARR	$X_S$	$R$	$N$	$\chi^2/dof$
	( <i>MJD</i> )	(3)	(sec)	( $\dot{M}_{Edd}$ )	( $\dot{M}_{Edd}$ )	(7)	( $r_s$ )	(9)	(10)	(11)
(1)	(2)		(4)	(5)	(6)		(8)			
00643949000	57188.77		1202	$0.050^{\pm 0.0013}$	$0.852^{\pm 0.046}$	$17.04^{\pm 0.98}$	$334^{\pm 15}$	$2.55^{\pm 0.10}$	$15.49^{\pm 1.19}$	69/51
		1	220	$0.055^{\pm 0.0015}$	$0.879^{\pm 0.043}$	$15.98^{\pm 0.85}$	$326^{\pm 13}$	$2.63^{\pm 0.09}$	$15.58^{\pm 1.22}$	66/51
		2	680	$0.057^{\pm 0.0014}$	$0.823^{\pm 0.045}$	$14.44^{\pm 0.71}$	$336^{\pm 13}$	$2.37^{\pm 0.10}$	$12.55^{\pm 1.09}$	72/51
		3	160	$0.041^{\pm 0.0015}$	$0.876^{\pm 0.043}$	$21.36^{\pm 0.91}$	$330^{\pm 13}$	$2.55^{\pm 0.09}$	$19.76^{\pm 1.51}$	59/51
00644520000	57191.03		1202	$0.124^{\pm 0.0022}$	$0.851^{\pm 0.028}$	$6.92^{\pm 0.22}$	$300^{\pm 11}$	$2.59^{\pm 0.10}$	$19.69^{\pm 0.89}$	338/281
		1	200	$0.131^{\pm 0.0022}$	$0.854^{\pm 0.037}$	$6.52^{\pm 0.39}$	$317^{\pm 10}$	$2.81^{\pm 0.11}$	$21.54^{\pm 1.17}$	56/51
		2	220	$0.109^{\pm 0.0026}$	$0.847^{\pm 0.053}$	$7.77^{\pm 0.45}$	$269^{\pm 10}$	$2.43^{\pm 0.12}$	$15.76^{\pm 1.34}$	61/51
		3	50	$0.096^{\pm 0.0025}$	$0.909^{\pm 0.049}$	$9.46^{\pm 0.51}$	$322^{\pm 11}$	$2.50^{\pm 0.13}$	$22.42^{\pm 1.81}$	71/51
		4	150	$0.124^{\pm 0.0037}$	$0.822^{\pm 0.045}$	$6.63^{\pm 0.42}$	$309^{\pm 11}$	$2.41^{\pm 0.11}$	$20.36^{\pm 1.15}$	57/51
00645176000	57193.56		542	$0.071^{\pm 0.0037}$	$1.577^{\pm 0.068}$	$22.15^{\pm 1.17}$	$220^{\pm 14}$	$2.14^{\pm 0.09}$	$14.43^{\pm 0.77}$	54/49
		1	150	$0.071^{\pm 0.0044}$	$1.582^{\pm 0.068}$	$22.28^{\pm 1.19}$	$218^{\pm 14}$	$2.15^{\pm 0.09}$	$14.04^{\pm 0.76}$	62/49
		2	260	$0.071^{\pm 0.0036}$	$1.553^{\pm 0.075}$	$21.87^{\pm 1.22}$	$230^{\pm 15}$	$2.13^{\pm 0.09}$	$14.93^{\pm 0.90}$	65/49
00646721000	57199.52		965	$0.134^{\pm 0.0207}$	$1.311^{\pm 0.047}$	$9.79^{\pm 0.17}$	$143^{\pm 8}$	$1.99^{\pm 0.09}$	$77.55^{\pm 3.29}$	35/51
		1	530	$0.136^{\pm 0.0212}$	$1.312^{\pm 0.051}$	$9.65^{\pm 0.22}$	$142^{\pm 8}$	$2.01^{\pm 0.10}$	$74.15^{\pm 3.37}$	37/51
		2	40	$0.133^{\pm 0.0194}$	$1.310^{\pm 0.042}$	$9.85^{\pm 0.18}$	$144^{\pm 9}$	$1.96^{\pm 0.09}$	$89.22^{\pm 2.54}$	36/51

TCAF fitted extracted parameters for time resolved BAT spectra in the energy range of 15 – 150 keV.

Note: First row in each spectra are TCAF model fitted spectral analysis results when entire data exposure including gaps are used.

The mass of the BH is frozen at  $10.6 M_{\odot}$  during the fitting.

**Table IV**

Obs ID	Day	$n_e$	$B$	$\Lambda_{syn}$	$t_{sync}$	$\Lambda_{Comp}$	$t_{Comp}$	$t_{inf}$	$t_{sync}/t_{inf}$	$t_{Comp}/t_{inf}$
	( <i>MJD</i> )	( $\times 10^{16}$ )	( <i>Gauss</i> )	( $\times 10^{-9}$ ergs/sec)	(s)	( $\times 10^{-3}$ ergs/s)	( $\times 10^{-3}$ s)	(s)	(10)	(11)
(1)	(2)	(3)	(4)	(5)	(6)	(7)	(8)	(9)		
00643949000	57188.77	1.07	$97^{\pm 3}$	1.01	81.16	0.25	12.34	1.22	66.48	10.10
00031403035	57189.62	1.51	$124^{\pm 4}$	1.62	50.51	0.39	9.06	1.04	48.44	8.69
00031403038	57191.01	2.05	$149^{\pm 4}$	2.35	34.91	0.45	8.38	0.91	38.33	9.20
00644520000	57191.03	1.59	$125^{\pm 4}$	1.66	49.24	0.69	4.97	1.04	47.30	4.77
00031403042	57192.16	2.28	$153^{\pm 5}$	2.50	32.79	0.53	6.74	1.05	31.24	6.42
00645176000	57193.56	6.67	$308^{\pm 12}$	10.12	8.17	0.67	7.34	0.65	12.53	11.20
00031403048	57194.16	34.38	$923^{\pm 44}$	90.14	0.91	3.07	2.79	0.28	3.21	9.85
00031403046	57194.54	25.57	$752^{\pm 25}$	59.91	1.37	2.52	3.04	0.33	4.09	9.10
00031403045	57195.08	16.55	$564^{\pm 19}$	33.71	2.43	1.49	4.46	0.41	5.92	10.91
00031403049	57195.35	7.28	$305^{\pm 9}$	9.82	8.34	0.53	8.38	0.64	12.99	13.04
00031403047	57195.41	3.03	$182^{\pm 7}$	3.49	23.46	0.50	7.50	0.88	26.59	8.49
00031403052	57196.89	2.56	$154^{\pm 5}$	4.21	19.49	1.67	9.49	0.99	19.71	1.95
00031403054	57197.21	11.29	$414^{\pm 14}$	18.22	4.51	0.84	6.25	0.51	8.85	12.33
00031403053	57197.33	14.49	$504^{\pm 16}$	26.91	3.04	1.66	3.65	0.44	6.99	8.83
00031403055	57198.00	28.70	$820^{\pm 29}$	71.15	1.51	5.06	1.60	0.31	3.78	5.26
00031403056	57198.02	17.84	$602^{\pm 24}$	38.33	2.13	3.78	1.86	0.38	5.59	4.86
00031403057	57198.15	13.94	$500^{\pm 18}$	26.41	3.09	2.35	2.63	0.46	6.72	5.72
00031403058	57198.93	16.65	$568^{\pm 26}$	34.21	2.40	3.31	2.03	0.41	5.89	4.99
00646721000	57199.55	21.38	$685^{\pm 25}$	49.64	1.65	4.31	1.76	0.34	4.84	5.16

Electron number density ( $n_e$ ) is in the unit of  $\times 10^{16} \text{ cm}^{-3}$ .

